Sensors & Actuators: B. Chemical 311 (2020) 127837

Contents lists available at ScienceDirect

Sensors and Actuators B: Chemical

journal homepage: www.elsevier.com/locate/snb

# Multiwavelength optical sensor based on a gradient photonic crystal with a hexagonal plasmonic array

Lina Dedelaite[a], Raul D. Rodriguez[b,*], Benjamin Schreiber[c], Arunas Ramanavicius[a], Dietrich R.T. Zahn[d], Evgeniya Sheremet[b]

[a] Department of Physical Chemistry, Faculty of Chemistry and Geosciences, Vilnius University, Naugarduko str. 24, LT- 03225, Vilnius, Lithuania
[b] Tomsk Polytechnic University, 30 Lenin Avenue, 634050, Tomsk, Russia
[c] Rudolf Virchow Center, University of Würzburg, Josef-Schneider-str. 2, 97080, Würzburg, Germany
[d] Semiconductor Physics, Chemnitz University of Technology, D-09107, Chemnitz, Germany

ARTICLE INFO

*Keywords:*
Optical sensor
Photonics
Surface-enhanced Raman spectroscopy
Photonic crystal

ABSTRACT

Sensitivity and versatility are characteristics that make a sensor device attractive for wide-spread applications in everyday life. Surface-enhanced Raman spectroscopy (SERS) is capable of providing the highest sensitivity, that of single-molecule detection, and excellent specificity due to its fingerprinting capability. However, conventional SERS substrates must be optimized to operate for a particular excitation wavelength. Here in this work, we achieve for the first time multiwavelength amplification with a hybrid plasmonic/photonic heterostructure integrating a gradient photonic crystal and an Ag nanotriangle array. We demonstrate the detection of ultrathin molecular layers showing a signal amplification for the typical laser wavelengths used in Raman spectroscopy detection. By combining photonics and plasmonics in a single silicon chip, we expand multiwavelength- and spatially-selective ultra-sensitive detection to a wide range of applications from biomedicine to safety.

## 1. Introduction

Raman spectroscopy is a valuable tool used for the chemical and structural analysis in different fields ranging from biomedicine to high-speed analysis in material sciences [1–3]. With minimum sample preparation, it is possible to determine a material's composition, obtain structural information, and concentration [4]. Raman spectroscopy has even made its way to the operating room, assisting doctors during brain surgery [5]. However, Raman signal is very low due to the poor efficiency of this inelastic light scattering process. For substances in which the analyte of interest appears at extremely low concentrations, it is close to impossible to obtain a reasonable signal that allows analyte detection. Here comes surface-enhanced Raman spectroscopy (SERS) that with the use of plasmonic nanoparticles, usually gold or silver, the Raman signal can be enhanced by a factor of up to $10^{15}$ [6]. To enhance the Raman signal, the metal nanoparticles have to be exposed to laser excitation. The best conditions for enhancement occur when the excitation wavelength matches the resonance excitation frequency of the localized surface plasmon resonance (LSPR) of the metal nanostructures [7]. An additional level of enhancement can be accessed when the Raman laser excitation matches the optical transition energy of the analyte under investigation [8]. Fulfilling this latter condition gives rise to surface-enhanced resonant Raman spectroscopy (SERRS) as elegantly demonstrated for carbon nanotubes by Dresselhaus and Kneipp in early 2000 [7,9]. The LSPR depends on the metal composition, size, shape, and arrangement of the plasmonic nanostructures [10]. Conventional plasmonic SERS substrates are in resonance within a relatively narrow wavelength range. Therefore, to produce a significant Raman signal enhancement for materials with different optical absorption we must use optimized SERS substrates for a particular sample and laser excitation. In this work, we aim to demonstrate an alternative method to obtain broadband enhancement of the Raman signal by integrating SERS with a gradient photonic crystal (GPC). The integration of different materials for SERS applications is an evolving topic. This includes recent developments in hybrid SERS platforms with the combination of plasmonic nanoparticles with reduced graphene oxide and cicada wings, or 3D plasmonic nanostructures separated by $WS_2$ bilayers [11,12].

Over the years, photonic crystals (PC) drew interest due to the easy and controllable fabrication process in which layers of defined optical properties (with an effective refractive index) and thickness can be achieved. Moreover, the PC large surface-area and compatibility with other materials and molecules make it popular among chemical sensors [13,14], biosensors [15,16], in optoelectronics [17], and other

---

* Corresponding author.
*E-mail address:* raul@tpu.ru (R.D. Rodriguez).

https://doi.org/10.1016/j.snb.2020.127837
Received 4 October 2019; Received in revised form 7 January 2020; Accepted 5 February 2020

applications. Even a single layer of porous silicon (on silicon) behaves like a Fabry-Pérot interferometer which in the reflectivity spectrum appears as constructive and destructive interference by light traveling (and reflecting) from air to the porous silicon layer, and from porous to crystalline silicon [17,18]. One-dimensional photonic crystals can be readily fabricated by electrochemically etching layers of porous silicon and at the same time alternating the layers porosity and thickness by switching current density and etching time [19]. This is possible because of complicated etching mechanism where electrochemical reaction is concentrated at the porous silicon - crystalline silicon interface and obtained uniform pores are passivated with Si-H, Si-$H_2$, and Si-$H_3$ groups. Therefore, reaction keeps moving deeper into silicon substrate without affecting already formed pores [20]. Porous silicon (one-dimensional photonic crystal) exhibits a photonic bandgap (stopband) at which a specific range of wavelengths are highly reflected. Due to that, PC can be used as optical bandwidth filters [21]. It was shown that the unique properties of the PC can be utilized to enhance Stokes emission [21–23] including the dual amplification by integrating with plasmonics [19,24]. The explanation of enhanced Raman scattering in the PC can be understood by considering two mechanisms. First, the PC substrate porosity leads to high optical intensities and increase in Raman scattering. This occurs because pores with size below excitation wavelength λ can spatially confine and amplify the electromagnetic field due to photon-trapping inside and among pores [25]. Secondly, and the most widely-accepted explanation, the periodicity of Si layers makes PC a distributed Bragg reflector (DBR). In the reflectivity spectrum, the photonic bandgap that corresponds to slow light offers the possibility to increase light-matter interaction. In the end, such photonic crystal increases the chances of Raman scattering [22]. A PC based on porous silicon is prepared by electrochemical etching using a Si wafer and Pt mesh as the electrodes to create a homogeneous electric field. The concept of gradient PC (GPC) can be realized by using an asymmetric electrode configuration where the counter electrode is a platinum wire instead of a mesh [20] as shown in Fig. 1a. This configuration induces a current density gradient throughout the electrolyte and the silicon wafer (Fig. 1b). Obtained gradient is directly responsible for pore diameter, porosity, and layer thickness variations. The spatial changes of these structural properties result in a gradient photonic crystal [20] with a spatially-dependent optical bandgap. Our hypothesis is that this gradient structure may allow having one substrate that has resonances with different lasers and molecules for SERS applications. Having such a “multiwavelength” substrate helps with higher reproducibility [26]. Increased reproducibility is expected since the same sample and substrate can be used under different excitation conditions. This versatility should minimize uncertainties due to multiple sample preparation required for different substrates individually-optimized for a particular wavelength.

The SERS enhancement is achieved with the integration of a hexagonal array of plasmonic nanotriangles fabricated on the GPC surface by nanosphere lithography (NSL) as shown previously [19]. This method has increasingly attracted interest due to its easy and simple use, low-cost, and potential to manufacture homogeneous nanostructures [19,27,28]. Our approach combines top-down and bottom-up fabrication through a two-step process. The first is monolayer formation from the colloidal solution at the water-air interface and its deposition as a mask on the substrate of choice. Usually, polystyrene (PS) nanospheres are used for this step. This step has the advantages of affordable materials and simple process. The second step is the deposition of a metal on the PS mask layer and then the mask removal that leaves a layer of ordered nanoclusters (mask interstices) on the GPC surface. By using the NSL method, triangular shaped nanoparticles are usually formed. By doubling or tripling the mask layer more complicated structures can also be achieved [29,30].

In this work, we show a gradient photonic crystal with a silver nanotriangles array as a multipurpose SERS substrate that incorporates an additional interference enhancement due to GPC.

## 2. Materials and methods

### 2.1. Materials

Cobalt phthalocyanine (CoPc) and hydrogen fluoride 48 % (HF) were purchased from Sigma-Aldrich. A polished silicon wafer ((100) orientation, p-type), which was used as a substrate, was purchased from LG Siltron Inc. The HF etching solution was prepared by mixing 50 % aqueous HF solution with 15 % ethanol HF solution ratio 1:1, later called HF etching solution. The substrates were cleaned in an ultrasonic bath first in isopropanol, followed by acetone, ethanol, and finally with deionized ultrapure water (Milli-Q) for 5 min each. For nanosphere lithography, water suspensions with polystyrene spheres of 450 nm diameter with carboxyl functional groups on their surface were obtained from Postnova Analytics GmbH (Germany). Before deposition, the polystyrene aqueous suspension was diluted 1:1 vol ratio with ethanol and placed in an ultrasonic bath for 2 min to disperse the spheres in the solution homogeneously. Metal deposition was carried out using 99.9 % silver (Ag) metal which was purchased from MaTecK GmbH (Germany).

### 2.2. Instrumentation

A gradient photonic crystal (GPC) was etched in a two-electrode cell where the silicon (p-type, (100)) wafer was used as a working electrode and a platinum wire as a counter electrode. Etching process was controlled using a power supply KORAD KA3005p. The surface of the photonic crystal and photonic crystal with metal nanotriangles were imaged using atomic force microscopy (AFM). An OmegaScope SPM

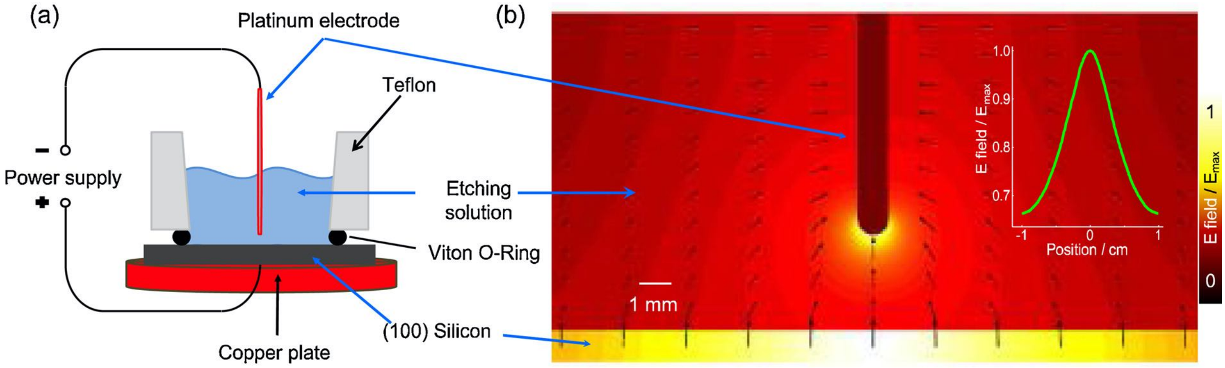

**Fig. 1.** a) Sketch illustrating the different components of the electrochemical cell for silicon wafer etching. b) Simulation of the normalized electric field distribution made by the tip of a Pt electrode in the electrochemical cell. Inset shows a cross-section profile of the electric field on the plane of the silicon surface showing the spatial changes in the electric field.

(AIST-NT) was used in tapping mode with conventional silicon cantilevers. A FEI Nova NanoSEM 200 SEM was used to obtain images of the prepared substrates on silicon with accelerating voltages in the range of 5 kV–15 kV. Reflectance measurements were performed with a Woollam VASE ellipsometer under ambient conditions. The spot size of the light was approximately 3 mm. If not stated otherwise, the incidence angle of s-polarized light was 19°. For reflectance mapping, Woollam M2000-Solar was used in the spectral range from 0.73 eV to 5.0 eV. The spot size of this ellipsometer at 75° illumination has an elliptical shape with a major axis size of 560 μm.

Raman spectroscopy experiments were performed with a micro-Raman spectrometer LabRam HR800 (HORIBA). Two excitation laser lines were used: 514.7 nm solid-state laser (Coherent) and 632.8 nm HeNe laser (Siemens). The laser intensity measured at the sample was set to 3 mW and 20 mW for the 514.7 nm and 632.8 nm, respectively. The laser light filtered by a plasma filter was focused onto the sample and had a laser spot size of about 3 μm with a 10x objective (numerical aperture, N.A. = 0.25). The laser excitation and signal collection were in the back-scattering configuration.

## 3. Results and discussion

### 3.1. Preparation of SERS substrates

#### 3.1.1. Gradient photonic crystal

We used a two-electrode cell sketched in Fig. 1a to fabricate gradient photonic crystals. Silicon wafers were etched in a HF solution with a Pt electrode wire with 1 mm diameter centered on top with 3 mm distance from the wafer. Finite element method (COMSOL Multiphysics v4.4.) simulation results of the normalized electric field for this configuration are shown in Fig. 1b. For the simulation, a voltage was applied between the silicon sheet (+) and platinum wire (−) immersed in a solution with an effective relative permittivity of 58. The simulation shows an electric field gradient marked by arrows. The cross-section of the electric field along the silicon surface shows a gaussian profile which corresponds with the etching rate on the silicon surface. Experimentally, the GPCs were made as a function of time and current while the potential bias remained constant. In Fig. 2a, we show the current variation *vs.* time (etching graph) where two different current densities of 50 mA/cm$^2$ and 13 mA/cm$^2$ were set for 5.9 s and 9.5 s respectively with breaks in-between of 5 s for 10 cycles. This periodic etching allowed us to obtain the sample shown in Fig. 2b.

The current density decreases outwards from the platinum wire tip following the electric field as it is reflected in Fig. 1b; which in turn makes the concentric gradient photonic crystal with a varying photonic bandgap in Fig. 2b. In Fig. 2c we show a cross-sectional view of the sample around the crack marked in Fig. 2b. Fig. 2c, obtained by scanning electron microscopy (SEM), evidences the layer structure of the sample. The thicker layer of ~131 nm was obtained by setting the current density to 50 mA/cm$^2$ for 5.9 s. The thinner layer of ~94 nm resulted from a current density of 13 mA/cm$^2$ applied during 9.5 s. In Fig. 2c, it is also visible that in the thicker layer the pores are denser than in the thinner layers. Moreover, a porosity gradient between layers was avoided by establishing a delay time between current changes as visible from the etching graph in Fig. 2a. In addition, the layer porosity changes as the distance from the counter electrode increases. All these factors determine the photonic bandgap. The PCs photonic bandgap was optimized by controlling the fabrication process, in particular, the current density and etching time (Fig. S1), and using formula: $n_1 \cdot d_1 = n_2 \cdot d_2 = \lambda/4$, where $n$ is the refractive index, $d$ – porous silicon layer thickness and $\lambda$ - wavelength. This tunability of the PCs bandgap allows us to be in resonance with different lasers and molecules for SERS enhancement in one single-substrate.

Fig. 3 depicts the reflectivity changes from blue (455 nm) to green (532 nm) and then to red (635 nm) when going from the area where the platinum electrode was set to outwards. We observed that by increasing the current, the layer porosity as well as pore size increased. We also found that increasing the etching time resulted in a layer thickness increase.

These results summarized in Fig. S1 are in agreement with previous reports [20,31]. Notice that the cross-sectional SEM image in Fig. 2c is only representative of that marked location of the GPC. The layers' porosity and thickness change radially as does the color of the sample in Fig. 2b. Therefore, the refractive index also changes as a function of position from the Pt tip electrode. A detailed cross-sectional SEM investigation of the GPC at different locations should be pursued in follow-up work. In particular, the dependence of GPC radial periodicity (and refractive index) on the electrochemical etching conditions (current pulse time, amplitude, and Pt-Si distance) could allow producing plasmonic-photonic samples optimized for more sophisticated

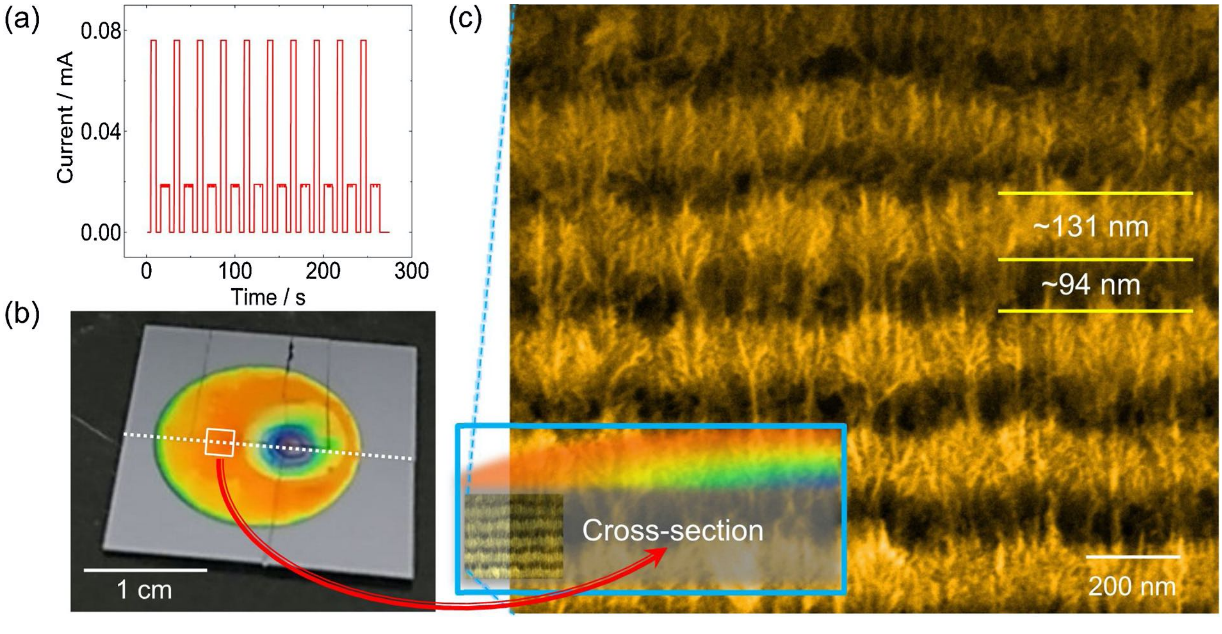

**Fig. 2.** (a) Current variation *vs.* time (etching graph). (b) Photography picture showing the color gradient of a GPC sample. (c) SEM cross-sectional image of the GPC fragment at the marked area in b), with the inset figure illustrating the cross-section view used in SEM.

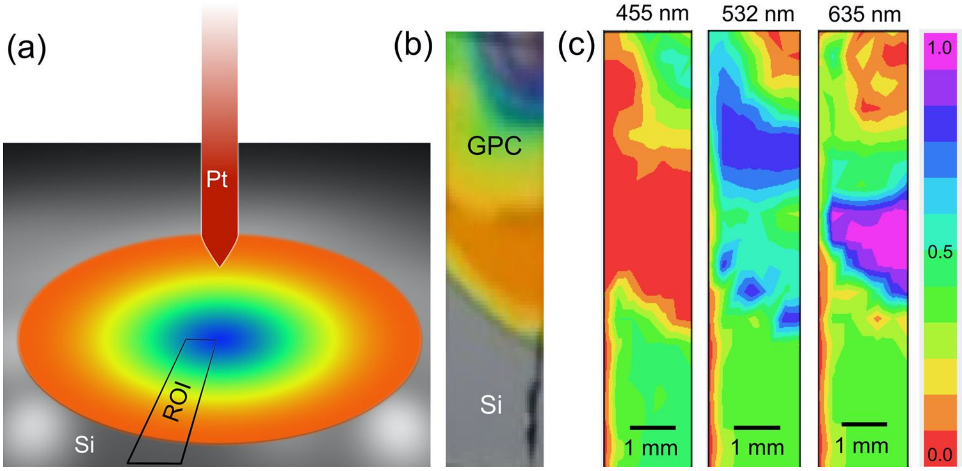

**Fig. 3.** (a) Sketch of the GPC sample with the fragment region of interest (ROI) marked by a rectangle. (b) Fragment of the gradient photonic crystal (optical photograph). (c) Reflectivity mapping of the same fragment at 455 nm, 532 nm, and 635 nm wavelengths.

applications like in odor compasses [32].

### 3.1.2. Nanotriangle arrays by nanosphere lithography

Deposition of metal nanotriangles was performed by nanosphere lithography (NSL). For this, the Vogel method was used where a 450 nm polystyrene nanosphere monolayer is formed due to the capillary forces at the water-air interface (Fig. S2a). This monolayer is then transferred onto the final substrate support where it adheres by van der Waals forces [33,34]. The monolayer was then allowed to dry and 0.1 g of silver was deposited on all the substrates simultaneously in a thermal evaporation chamber with a base pressure of *ca.* $8{\cdot}10^{-6}$ mbar (Fig. S2b) covering all the substrates with 64 nm silver film as shown by AFM results in Fig. S3. Removal of polystyrene spheres, using adhesive-tape, resulted in 55 nm thick and 120 nm wide nanotriangles as shown by AFM results below. During this step, the nanospheres work as a shadow mask where metal atoms can reach the substrate only through interstices between three neighboring spheres forming triangle-shape pyramids. These triangular pyramids stay on the substrate even after removing the nanosphere monolayer. After the deposition of nanotriangles no visible change of color was observed. In Fig. 4a, b, the Ag nanotriangles (AgNT) arranged in hexagonal arrays are visible by SEM. We notice in the zoomed-out image (Fig. 4a) that some defects become visible. These minor defects appear due to the monolayer formation. Nevertheless, this method is still adequate for many applications, unless it requires extremely high accuracy [35]. AFM was performed on the silver nanostructures to evaluate their 3D shape (Fig. 4c). We also determined the GPC surface roughness and found that it changes radially from the middle with 1.8 nm up to 25 nm at the outer periphery. From the AFM image (Fig. 4c) and the cross-section (Fig. 4d) on the two triangles the shape of the nanoparticles can be described as a truncated tetrahedron. The description of this shape would be a regular tetrahedron with a top “sliced off” parallel to the base of the structure [36]. The height of each pyramid is (55 ± 1) nm and width of (120 ± 1) nm. These numbers depend on the diameter of the polystyrene nanospheres used as a mask during metal deposition [29].

## 3.2. GPC substrate with AgNTs

### 3.2.1. The reflectance of GPC with AgNTs

The optical properties of GPC and AgNT on GPC were analyzed to understand the electromagnetic (EM) enhancement mechanism of SERS [7,29,37]. As EM enhancement mechanism states that if resonance conditions are met when the collective oscillation of conducting electrons will absorb and scatter photons. It is known that due to plasmon resonance excitation a strongly amplified local EM will be obtained at the nanoparticle surface. Using optical spectroscopy in either transmission or reflection mode the scattered and absorbed light can be measured [38].

In Fig. 5, reflectance measurements of the GPC area reveal a photonic bandgap at ∼635 nm, which was observed in the presence and absence of AgNTs. The spectroscopic analysis shows a GPC reflectance maximum ($R_{max}$) of 0.99 and a full-width half-maximum (FWHM) of the stop band of up to 156 nm, which means that at that area the GPC reflects in a relatively wide spectral range. This result can be based on the influence of a large $\Delta n$ between the layers ($n_1 = 1.72$ @13.3 mA/cm$^2$, $n_2 = 1.21$ @50 mA/cm$^2$, for the red GPC region) that makes this photonic crystal an optimal Bragg reflector [39]. By moving closer to the middle region, the $R_{max}$ decreases due to the decrease in $\Delta n$, although it still stays relatively high at 455 nm with $R_{max} = 0.54$ (Fig. 3). After the deposition of AgNTs the reflectance was measured in the same area.

We observed that the $R_{max}$ shifts towards longer wavelengths and a broad dip appears in the bandgap around 750 nm. This dip appears due to the increased scattering and absorption by the AgNTs and the localization of the electromagnetic field, which occurs at the interface between the two structures. This reflectance decrease is observed only when the plasmonic resonance of the AgNTs matches the resonance of the photonic bandgap [40]. The advantage of this system is that the localized and amplified fields can interact with the materials deposited on the surface and enhance their Raman signal in a combinational way.

### 3.2.2. Detection of CoPc with surface-enhanced Raman spectroscopy

To evaluate the substrates fabricated for multiwavelength SERS application, ultrathin (2 nm) layer of CoPc was deposited on GPC with AgNTs (GPC/AgNTs) and silicon. To perform a proper comparison of the electric field enhancement, the CoPc layer was deposited simultaneously on all substrates using organic molecular beam deposition (OMBD) ensuring the same analyte for all regions of interest which is essential for comparison purposes [41]. After CoPc deposition, Raman spectra were recorded using a LabRam spectrometer equipped with a 10x (0.25 N.A.) objective to average the signal over micrometer size areas. For the comparison of the multipurpose GPC/AgNT SERS substrate, we used two laser excitations, namely green (514.7 nm) and red (632.8 nm).

In Fig. 6, we show the Raman spectra of 2 nm CoPc taken from silicon (Si), Si with silver nanotriangles (Si/AgNTs), and from three different areas of GPC and GPC/AgNTs: blue (B GPC and B GPC/AgNTs), green (G GPC and G GPC/AgNTs), and red (R GPC and R GPC/AgNTs). The CoPc molecule has high optical absorbance in the red spectral range and comparative low in the green. This implies that resonance

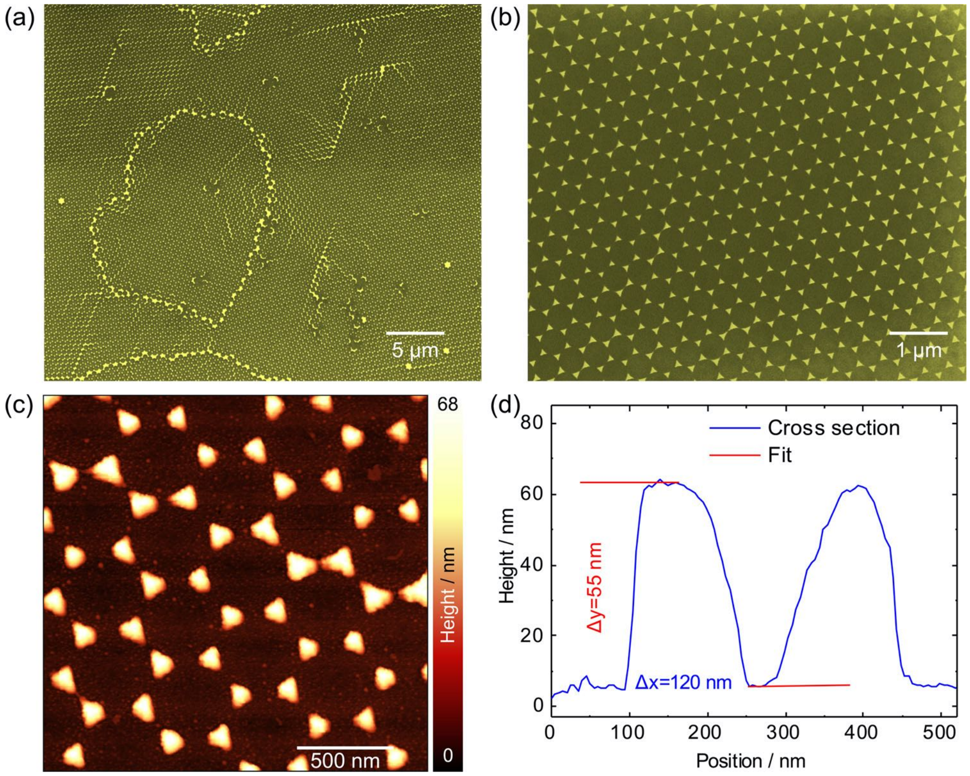

**Fig. 4.** (a, b) SEM image of silver metal nanotriangles on GPC surface formed with nanosphere lithography at two different magnifications, (c) AFM image of Ag nanoclusters on the GPC and (d) cross-section of two nanotriangles.

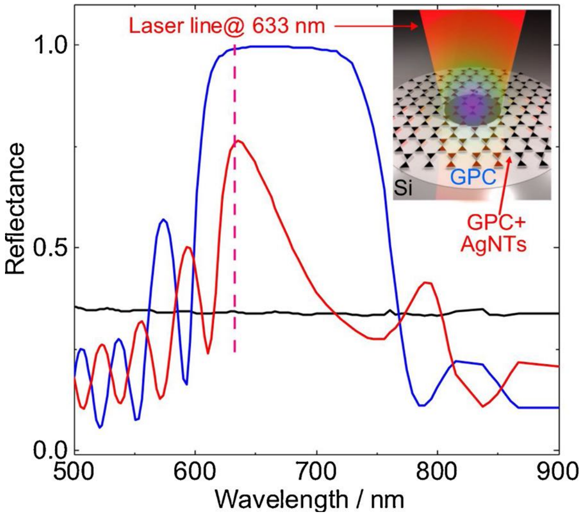

**Fig. 5.** Reflectance of GPC (blue) and GPC with AgNTs (red) showing a peak around 635 nm, with the dashed line at 633 nm marking the wavelength of the red laser. The black curve is the spectra of Si as reference. (For interpretation of the references to colour in this figure legend, the reader is referred to the web version of this article).

with the red laser results in higher Raman signals than that when the sample is excited by the green laser [40,42,43]. There are some differences in the Raman spectra too, not just in the overall intensity but also in the lineshape and intensity ratios. These spectral differences are related to resonance conditions like previously reported for CuPc [44]. For all spectra, the most intense band is located at 1539 $\mathrm{cm}^{-1}$, which corresponds to C—N vibrations. Therefore, the enhancement factors were calculated using the peak intensity of this band (Fig. 6d), taking the signal from the molecule on the silicon substrate as a reference. As seen in Fig. 6b, the Raman signal of 2 nm CoPc on silicon is low even when it fits the resonant Raman scattering conditions under red laser excitation.

The Raman signal taken from Si/AgNTs increases 245 times using the red laser and only 35 using the green that is related to the position of the localized surface plasmon. Thus, depositing silver nanotriangles on the silicon substrate already amplifies the Raman signal by at least a factor of 35. By comparing the Raman signal of CoPc at different areas of the GPC we found a significant signal enhancement due to optical interference [45–47] especially in the red area, and the enhancement is consistent with the reflectance imaging result [48]. Photonic crystals are already known as good Raman substrates since it is possible to tune the Raman signal by changing the wavelength of the laser and/or using different chemical compounds [49]. We observed that the Raman signal of CoPc increases up to $10^5$ – $10^6$ times when AgNTs are deposited on the photonic crystal. In this case, nanosphere lithography allows obtaining particles with a triangular shape that have field enhancement at the tips. Additionally, the influence of metal nanoparticles is supported by the concentration of the electromagnetic field on the photonic crystal surface leading to their synergistic enhancement effect [50]. Moreover, the 1D photonic crystal has a porous surface that increases the Raman scattering in addition to being a Bragg reflector that increases the local amplification of the laser light [22,23]. The signal enhancement could also be optimized for other spectral regions by changing the deposition parameters such as substrate tilt angle or nanosphere size [29] as well as the metal composition from silver (optimal for visible range) to another one like Au for IR applications, and Al or In for the UV range.

CoPc has vibrational modes that span a spectral range of over 1000 $\mathrm{cm}^{-1}$ (Fig. 7a, b). This allows us to represent the Raman signal enhancement for different spectral regions illustrating the multi-wavelength enhancement. The spectral comparison is shown in Fig. 7a, b for red and green laser excitations. These spectra were obtained from Raman hyperspectral maps. The locations where the spectra were taken are marked by numbers in Fig. 7c, d. The Raman intensity ratio between

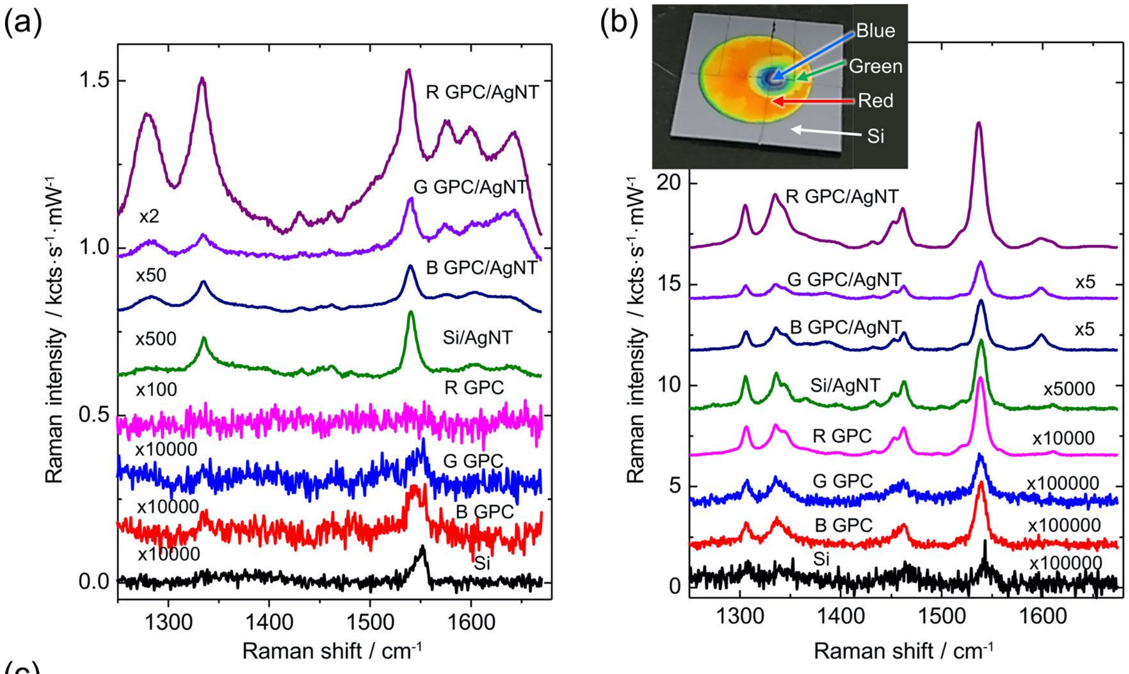

(c)

| *λ*, nm | Si | B GPC | G GPC | R GPC | Si/AgNT | B GPC/AgNT | G GPC/AgNT | R GPC/AgNT |
|---|---|---|---|---|---|---|---|---|
| 514.7 | 1 | 1 | 1 | - | 35 | 2476 | 8133 | 43999 |
| 632.8 | 1 | 11 | 8 | 136 | 245 | 177268 | 130934 | 2209171 |

**Fig. 6.** Raman spectra of 2 nm CoPc on silicon, silicon with AgNT and three areas of GPC and GPC/AgNT: blue area (B GPC and B GPC/AgNT), green area (G GPC and G GPC/AgNT), red area (R GPC and R GPC/AgNT). Spectra were taken using two different laser excitations: (a) 514.7 nm and (b) 632.8 nm. Spectra were rescaled as followed by the factor shown on top of each spectrum. The inset of Fig. 6b is an image of the sample with the regions of interest marked by arrows. (c) Enhancement factor (EF) was calculated for the most prominent peak of CoPc at 1539 $cm^{-1}$. (For interpretation of the references to colour in this figure legend, the reader is referred to the web version of this article).

a low and a high wavenumber mode provide us information on the spatial distribution with different spectral enhancement by the GPC-AgNTs. The low wavenumber mode is located at 682 $cm^{-1}$, *i.e.*at*ca.*552 nm and 667 nm for 532 nm and 638 nm excitation, respectively. The high wavenumber mode is located at 1539 $cm^{-1}$, *i.e. ca.*580 nm and 708 nm (for green and red excitation, respectively).

We show the Raman imaging results in Fig. 7c, d for the two laser excitations we studied. The Raman peaks used for the intensity ratio images are marked by arrows and rectangles in Fig. 7a, b. The images have two parts - in the upper right side, the PS spheres were removed leaving behind a hexagonal Ag nanocluster pattern on top of the GPC. In the lower-left side the metallic layer remained intact making a metal film on nanospheres (MFON) that gives SERS enhancement only. The inset in Fig. 7c shows a SEM image of this interface. The first observation from the Raman intensity ratio maps is the radial periodicity, starting from the top-left towards bottom-right. This periodicity is not visible for the lower-left side of the Raman maps since that region remained covered with the metal-coated nanosphere layer masking the GPC below. The ultrathin 2 nm thick CoPc layer was deposited by organic molecular beam deposition and thus it is expected to uniformly cover the whole substrate. Therefore, we attribute the spatial distribution of intensity ratios to the different optical response modulated by the photonic crystal. The other interesting observation from Fig. 7c, d and further confirmation of the multiwavelength-enhancement in a single-chip is the difference between the spatial distribution on the same sample obtained under two different laser excitations. This combination between plasmonic and photonic enhancement can result in ultra-high sensitivity at the zeptogram detection level [51], and now showed another degree of freedom with the multiwavelength radial distribution. Signal enhancement reproducibility is a very important issue in SERS. In this work, reproducibility was verified with several substrates prepared following the same procedure and found similar results. An additional advantage of our method is that we combine two well-established and reproducible technologies into one. On the one hand, the nanosphere lithography approach is accepted to be one of the easiest methods that offers the best large-scale batch-to-batch reproducibility for SERS. On the other hand, the Raman enhancement approach based on a 1D photonic crystal is well-established and it even lacks the uncertainty issues related to SERS substrates as shown by different sensing applications (see Refs. 13–24). The spatially-selective spectral enhancement can be exploited in the analysis of complex multicomponent systems such as biological materials. Consider tissue analysis that usually requires pre-processing with the separation into different components. By using our GPC/AgNT sensor we could identify cytochrome C [52] and cancer-related exosomes [53]. Such investigation can explain the mechanism of cell apoptosis resistance in tumor cells, metastasis, and cancer diagnostics while avoiding major challenges with sample preparation and purification [54].

## 4. Conclusions

We developed a gradient photonic crystal with silver nanotriangles as a multipurpose SERS substrate that integrates interference and plasmonic enhancement. We used a 2 nm of cobalt phthalocyanine (CoPc) layer as a Raman active analyte deposited simultaneously on all substrates. Raman spectroscopy, atomic force microscopy, and

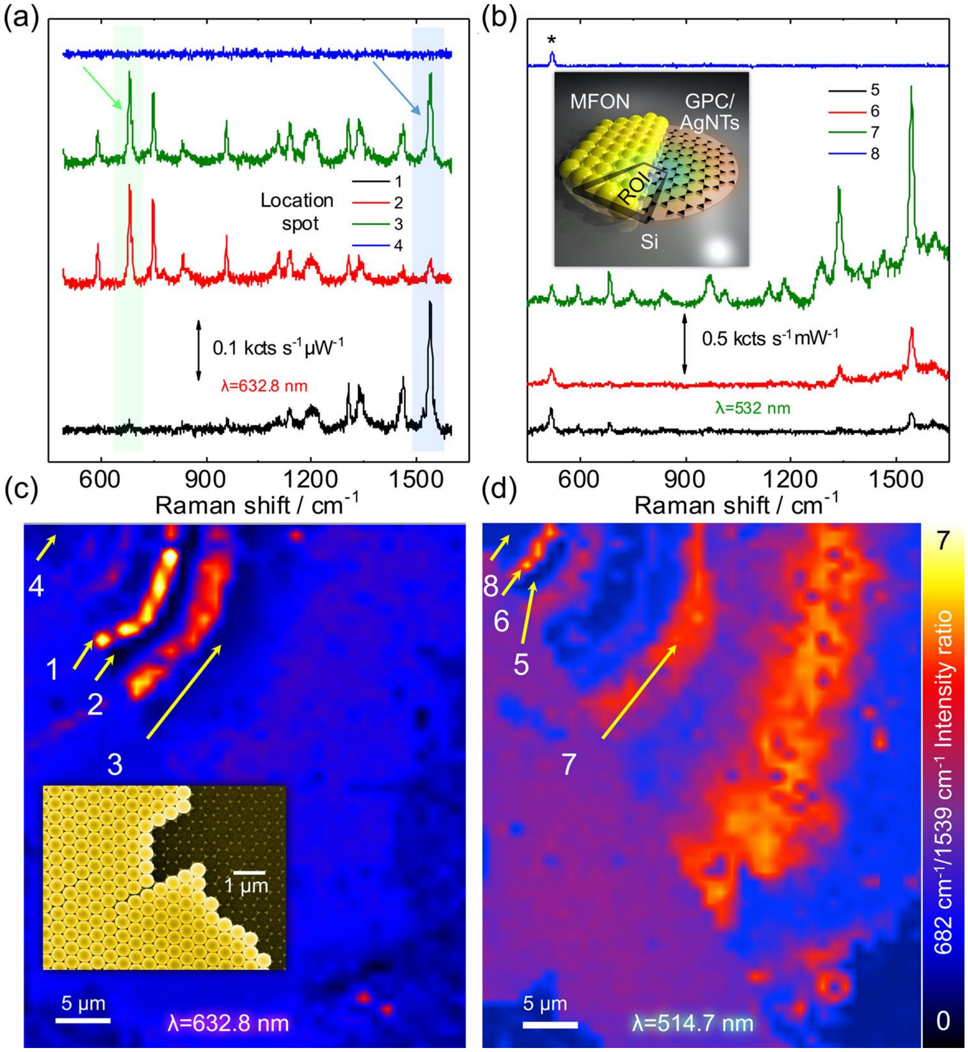

**Fig. 7.** Raman spectra under (a) red and (b) green laser excitations obtained from different locations of the GPC/AgNTs sample. These locations are indicated by numbers and arrows in the Raman maps. The maps in (c) and (d) were constructed from the Raman intensity ratio between low ($682\,cm^{-1}$) and high ($1539\,cm^{-1}$) wavenumber Raman modes of CoPc. Each map was obtained under the laser excitation indicated on each figure. The left-bottom side in the maps was a part of the sample with metal-coated nanospheres (MFON) left on the substrate, as indicated by the SEM image placed on (c). The asterisk-marked peak in (b) comes from the Si substrate. The inset in Fig. 7b is a sketch (non-scaled) of the sample structure and region of interest scanned in Raman imaging. (For interpretation of the references to colour in this figure legend, the reader is referred to the web version of this article).

reflectivity spot measurements, as well as imaging, were used to characterize the structural and optical properties of our hybrid photonic crystal-plasmonic substrates. Our results show that in a single silicon chip, robustly and inexpensively, multiwavelength optimization can be achieved for sensing applications allowing ultrasensitive detection and high specificity.

## Author contributions

L.D. performed the fabrication of the GPC and AgNTs. L.D. and R.D.R. performed the experiments and analyses based on Raman spectroscopy, and electron and atomic force microscopies. R.D.R. conceived and supervised the GPC/AgNTs SERS work. B.S. contributed with the finite-element method simulations. The manuscript draft was written jointly by L.D. and R.D.R. with input from B.S., A.R., D.R.T.Z., and E.S.

## Declaration of competing interest

The authors declare that they have no known competing financial interests or personal relationships that could have appeared to influence the work reported in this paper.

## Acknowledgments

We thank Axel Fechner for precious assistance with the PS fabrication, Martin Fränzl for initiating the research on PS, and to Stefan Moras, Mahfujur Rahaman, and Ashutosh Mukherjee for help with nanosphere lithography, CoPc deposition, and AFM. This work is supported by the Erasmus+ programme of the European Union and the Russian Science Foundation grant (project number 19-75-10046).

## Appendix A. Supplementary data

Supplementary material related to this article can be found, in the online version, at doi:https://doi.org/10.1016/j.snb.2020.127837.

## References

[1] E. Lenzi, D. Jimenez de Aberasturi, L.M. Liz-Marzán, Surface-enhanced Raman scattering tags for three-dimensional bioimaging and biomarker detection, ACS Sens. 4 (2019) 1126–1137.

[2] P. Reokrungruang, I. Chatnuntawech, T. Dharakul, S. Bamrungsap, A simple paper-based surface enhanced Raman scattering (SERS) platform and magnetic separation for cancer screening, Sens. Actuators B Chem. 285 (2019) 462–469, https://doi.org/10.1016/j.snb.2019.01.090.

[3] N.C. Lindquist, C.D.L. de Albuquerque, R.G. Sobral-Filho, I. Paci, A.G. Brolo, High-speed imaging of surface-enhanced Raman scattering fluctuations from individual nanoparticles, Nat. Nanotechnol. (2019), https://doi.org/10.1038/s41565-019-0535-6.

[4] E. Smith, G. Dent, Modern Raman Spectroscopy: A Practical Approach, Wiley, 2019.

[5] M. Jermyn, K. Mok, J. Mercier, J. Desroches, J. Pichette, K. Saint-Arnaud, L. Bernstein, M.-C. Guiot, K. Petrecca, F. Leblond, Intraoperative brain cancer detection with Raman spectroscopy in humans, Sci. Transl. Med. 7 (2015), https://doi.org/10.1126/scitranslmed.aaa2384 274ra19–274ra19.

[6] S. Schlücker, Surface-enhanced Raman spectroscopy: concepts and chemical

applications, Angew. Chemie Int. Ed. 53 (2014) 4756–4795, https://doi.org/10.1002/anie.201205748.

[7] M. Moskovits, Surface-enhanced spectroscopy, Rev. Mod. Phys. 57 (1985) 783–826, https://doi.org/10.1103/revmodphys.57.783.

[8] E.V. Efremov, F. Ariese, C. Gooijer, Achievements in resonance Raman spectroscopy review of a technique with a distinct analytical chemistry potential, Anal. Chim. Acta 606 (2008) 119–134.

[9] P. Corio, S.D.M. Brown, A. Marucci, M.A. Pimenta, K. Kneipp, G. Dresselhaus, M.S. Dresselhaus, Surface-enhanced resonant Raman spectroscopy of single-wall carbon nanotubes adsorbed on silver and gold surfaces, Phys. Rev. B 61 (2000) 13202–13211, https://doi.org/10.1103/physrevb.61.13202.

[10] M. Rycenga, C.M. Cobley, J. Zeng, W. Li, C.H. Moran, Q. Zhang, D. Qin, Y. Xia, Controlling the synthesis and assembly of silver nanostructures for plasmonic applications, Chem. Rev. 111 (2011) 3669–3712.

[11] W. Yang, Z. Li, Z. Lu, J. Yu, Y. Huo, B. Man, J. Pan, H. Si, S. Jiang, C. Zhang, Graphene-Ag nanoparticles-cicada wings hybrid system for obvious SERS performance and DNA molecular detection, Opt. Express 27 (2019) 3000–3013.

[12] Z. Lu, H. Si, Z. Li, J. Yu, Y. Liu, D. Feng, C. Zhang, W. Yang, B. Man, S. Jiang, Sensitive, reproducible, and stable 3D plasmonic hybrids with bilayer WS2 as nanospacer for SERS analysis, Opt. Express 26 (2018) 21626, https://doi.org/10.1364/oe.26.021626.

[13] C. Fenzl, T. Hirsch, O.S. Wolfbeis, Photonic crystals for chemical sensing and biosensing, Angew. Chemie Int. Ed. 53 (2014) 3318–3335, https://doi.org/10.1002/anie.201307828.

[14] N.I. Klyui, I.I. Ivanov, O.S. Kyslovets, L.V. Avksentyeva, V.A. Skryshevsky, Features of the use of optical reflection from thin porous silicon for detection of organic liquids, Sens. Actuators B Chem. 242 (2017) 1177–1185, https://doi.org/10.1016/j.snb.2016.09.124.

[15] M.B. de la Mora, M. Ocampo, R. Doti, J.E. Lugo, J. Faubert, Porous Silicon Biosensors, State of the Art in Biosensors - General Aspects, (2013), https://doi.org/10.5772/52975.

[16] O. Syshchyk, V.A. Skryshevsky, O.O. Soldatkin, A.P. Soldatkin, Enzyme biosensor systems based on porous silicon photoluminescence for detection of glucose, urea and heavy metals, Biosens. Bioelectron. 66 (2015) 89–94, https://doi.org/10.1016/j.bios.2014.10.075.

[17] K.F. Mak, J. Shan, Photonics and optoelectronics of 2D semiconductor transition metal dichalcogenides, Nat. Photonics 10 (2016) 216–226, https://doi.org/10.1038/nphoton.2015.282.

[18] D. Mangaiyarkarasi, M.B.H. Breese, O.Y. Sheng, K. Ansari, C. Vijila, D. Blackwood, Porous silicon-based Bragg reflectors and Fabry-Perot interference filters for photonic applications, Silicon Photonics. (2006), https://doi.org/10.1117/12.647316.

[19] M. Fränzl, S. Moras, O.D. Gordan, D.R.T. Zahn, Interaction of one-dimensional photonic crystals and metal nanoparticle arrays and its application for surface-enhanced raman spectroscopy, J. Phys. Chem. C. 122 (2018) 10153–10158.

[20] M.J. Sailor, Porous Silicon in Practice: Preparation, Characterization and Applications, John Wiley & Sons, 2012.

[21] C. Pacholski, Photonic crystal sensors based on porous silicon, Sensors 13 (2013) 4694–4713, https://doi.org/10.3390/s130404694.

[22] J.F. McMillan, M. Yu, D.-L. Kwong, C.W. Wong, Observation of spontaneous Raman scattering in silicon slow-light photonic crystal waveguides, Appl. Phys. Lett. 93 (2008) 251105, , https://doi.org/10.1063/1.3050457.

[23] H. Oda, K. Inoue, N. Ikeda, Y. Sugimoto, K. Asakawa, Observation of Raman scattering in GaAs photonic-crystal slab waveguides, Opt. Express 14 (2006) 6659, https://doi.org/10.1364/oe.14.006659.

[24] C. Liu, Z. Wang, E. Li, Z. Liang, S. Chakravarty, X. Xu, A.X. Wang, R.T. Chen, D. Fan, Electrokinetic manipulation integrated plasmonic-photonic hybrid Raman nanosensors with dually enhanced sensitivity, ACS Sens. 2 (2017) 346–353.

[25] L.-Y. Chen, X.-Y. Hou, D.-M. Huang, P.-H. Hao, F.-L. Zhang, X.-W. Feng, Y.-H. Qian, X. Wang, Optical study of photon-trapped porous silicon layer, J. Appl. Phys. 33 (1994) 1937–1943, https://doi.org/10.1143/jjap.33.1937.

[26] P.-Y. Wang, L.R. Clements, H. Thissen, S.-C. Hung, N.-C. Cheng, W.-B. Tsai, N.H. Voelcker, Screening the attachment and spreading of bone marrow-derived and adipose-derived mesenchymal stem cells on porous silicon gradients, RSC Adv. 2 (2012) 12857, https://doi.org/10.1039/c2ra21557h.

[27] X. Xu, Q. Yang, N. Wattanatorn, C. Zhao, N. Chiang, S.J. Jonas, P.S. Weiss, Multiple-patterning nanosphere lithography for fabricating periodic three-dimensional hierarchical nanostructures, ACS Nano 11 (2017) 10384–10391.

[28] P.V. Shanta, Q. Cheng, Graphene oxide nanoprisms for sensitive detection of environmentally important aromatic compounds with SERS, ACS Sens. 2 (2017) 817–827.

[29] C.L. Haynes, R.P. Van Duyne, Nanosphere Lithography: A versatile nanofabrication tool for studies of size-dependent nanoparticle optics, J. Phys. Chem. B 105 (2001) 5599–5611, https://doi.org/10.1021/jp010657m.

[30] P. Colson, C. Henrist, R. Cloots, Nanosphere lithography: a powerful method for the controlled manufacturing of nanomaterials, J. Nanomater. 2013 (2013) 1–19, https://doi.org/10.1155/2013/948510.

[31] P. Kumar, P. Huber, Effect of etching parameter on pore size and porosity of electrochemically formed nanoporous silicon, J. Nanomater. 2007 (2007) 1–4, https://doi.org/10.1155/2007/89718.

[32] W.J. Thrift, A. Cabuslay, A.B. Laird, S. Ranjbar, A.I. Hochbaum, R. Ragan, Surface-enhanced raman scattering-based odor compass: locating multiple chemical sources and pathogens, ACS Sens. (2019), https://doi.org/10.1021/acssensors.9b00809.

[33] N. Vogel, S. Goerres, K. Landfester, C.K. Weiss, A convenient method to produce close- and non-close-Packed monolayers using direct assembly at the air-water interface and subsequent plasma-induced size reduction, Macromol. Chem. Phys. 212 (2011) 1719–1734, https://doi.org/10.1002/macp.201100187.

[34] J.P. Mailoa, Y.S. Lee, T. Buonassisi, I. Kozinsky, Textured conducting glass by nanosphere lithography for increased light absorption in thin-film solar cells, J. Phys. D Appl. Phys. 47 (2014) 085105, , https://doi.org/10.1088/0022-3727/47/8/085105.

[35] W. Yuen, H. Wai, Nanosphere lithography for nitride semiconductors, Lithography (2010), https://doi.org/10.5772/8196.

[36] T.R. Jensen, G.C. Schatz, R.P. Van Duyne, Nanosphere lithography: surface plasmon resonance spectrum of a periodic array of silver nanoparticles by ultraviolet – visible extinction spectroscopy and electrodynamic modeling, J. Phys. Chem. B 103 (1999) 2394–2401, https://doi.org/10.1021/jp984406y.

[37] G.C. Schatz, R.P. Van Duyne, Electromagnetic mechanism of surface-enhanced spectroscopy, Handbook of Vibrational Spectroscopy, (2006), https://doi.org/10.1002/0470027320.s0601.

[38] C. Farcau, S. Astilean, Probing the unusual optical transmission of silver films deposited on two-dimensional regular arrays of polystyrene microspheres, J. Opt. A Pure Appl. Opt. 9 (2007) S345–S349, https://doi.org/10.1088/1464-4258/9/9/s10.

[39] S. Setzu, P. Ferrand, R. Romestain, Optical properties of multilayered porous silicon, Mater. Sci. Eng. B 69–70 (2000) 34–42, https://doi.org/10.1016/s0921-5107(99)00261-5.

[40] H. Liu, X. Sun, F. Yao, Y. Pei, F. Huang, H. Yuan, Y. Jiang, Optical magnetic field enhancement through coupling magnetic plasmons to Tamm plasmons, Opt. Express 20 (2012) 19160, https://doi.org/10.1364/oe.20.019160.

[41] R.D. Rodriguez, E. Sheremet, M. Nesterov, S. Moras, M. Rahaman, T. Weiss, M. Hietschold, D.R.T. Zahn, Aluminum and copper nanostructures for surface-enhanced Raman spectroscopy: a one-to-one comparison to silver and gold, Sens. Actuators B Chem. 262 (2018) 922–927, https://doi.org/10.1016/j.snb.2018.02.006.

[42] A.B. Djurišić, C.Y. Kwong, T.W. Lau, Z.T. Liu, H.S. Kwok, L.S.M. Lam, W.K. Chan, Spectroscopic ellipsometry of metal phthalocyanine thin films, Appl. Opt. 42 (2003) 6382, https://doi.org/10.1364/ao.42.006382.

[43] T. Birnbaum, T. Hahn, C. Martin, J. Kortus, M. Fronk, F. Lungwitz, D.R.T. Zahn, G. Salvan, Optical and magneto-optical properties of metal phthalocyanine and metal porphyrin thin films, J. Phys. Condens. Matter 26 (2014) 104201, , https://doi.org/10.1088/0953-8984/26/10/104201.

[44] A.J. Bovill, A.A. McConnell, J.A. Nimmo, W.E. Smith, Resonance Raman spectra of. alpha.-copper phthalocyanine, J. Phys. Chem. 90 (1986) 569–575, https://doi.org/10.1021/j100276a017.

[45] W.S. Bacsa, E. Pavlenko, V. Tishkova, Optical interference substrates for nanoparticles and two-dimensional materials, Nanomater. Nanotechnol. 3 (2013) 22, https://doi.org/10.5772/57464.

[46] G.A.N. Connell, R.J. Nemanich, C.C. Tsai, Interference enhanced Raman scattering from very thin absorbing films, Appl. Phys. Lett. 36 (1980) 31–33, https://doi.org/10.1063/1.91304.

[47] R.J. Nemanich, C.C. Tsai, G.A.N. Connell, Interference-enhanced Raman scattering of very thin titanium and titanium oxide films, Phys. Rev. Lett. 44 (1980) 273–276, https://doi.org/10.1103/physrevlett.44.273.

[48] Ľ. Vančo, M. Kadlečíková, J. Breza, M. Vojs, P. Michniak, M. Marton, Interference enhancement in SERS spectra of rhodamine 6G: relation to reflectance, Vib. Spectrosc. 90 (2017) 31–37, https://doi.org/10.1016/j.vibspec.2017.03.002.

[49] S.-M. Kim, W. Zhang, B.T. Cunningham, Coupling discrete metal nanoparticles to photonic crystal surface resonant modes and application to Raman spectroscopy, Opt. Express 18 (2010) 4300, https://doi.org/10.1364/oe.18.004300.

[50] A.G. Milekhin, N.A. Yeryukov, L.L. Sveshnikova, T.A. Duda, E.E. Rodyakina, V.A. Gridchin, E.S. Sheremet, D.R.T. Zahn, Combination of surface- and interference-enhanced Raman scattering by CuS nanocrystals on nanopatterned Au structures, Beilstein J. Nanotechnol. 6 (2015) 749–754.

[51] J. Proust, J. Martin, D. Gérard, J.-L. Bijeon, J. Plain, Detecting a zeptogram of pyridine with a hybrid plasmonic-photonic nanosensor, ACS Sens. 4 (2019) 586–594.

[52] C. Zang, J.A. Stevens, J.J. Link, L. Guo, L. Wang, D. Zhong, Ultrafast proteinquake dynamics in cytochrome c, J. Am. Chem. Soc. 131 (2009) 2846–2852.

[53] X. Zhang, X. Yuan, H. Shi, L. Wu, H. Qian, W. Xu, Exosomes in cancer: small particle, big player, J. Hematol. Oncol. 8 (2015) 83.

[54] Y.H. Soung, S. Ford, V. Zhang, J. Chung, Exosomes in cancer diagnostics, Cancers 9 (2017), https://doi.org/10.3390/cancers9010008.

Dr. Lina Dedelaite is from Vilnius, Lithuania. She received her BS and MS degree in Chemistry from Vilnius University in 2011 and 2013, respectively. There she received her Ph.D. in physical chemistry in 2018. During her studies, she did several scientific researches abroad, one of them was in Selcuk University in Konya, Turkey and other research visits in Chemnitz University of Technology in Chemnitz, Germany where she got interested in Raman spectroscopy. Her scientific interest focuses on developing SERS substrates, analysis, and new applications.

Prof. Dr. Raul D. Rodriguez received a Ph.D. in Physics and Chemistry of Nanomaterials in 2009 with the highest honors at the Institut des NanoSciences de Paris, Pierre et Marie Curie University (Sorbonne Universités) Paris, France. In 2011, he joined the DFG Research Unit Sensoric Micro- and Nano-Systems (SMINT) in the Semiconductor Physics group at TU Chemnitz, Germany. His experience in SMINT included the implementation and development of novel methods for nanoscale characterization (TERS, CSAFM, KPFM, and nano-Vis). He was appointed in 2017 as a Full Professor at Tomsk Polytechnic University, Russia. He is focusing on novel plasmonic and 2D nanomaterials for technological developments including biomedicine, optoelectronics, energy, and safety applications.

Dr. Benjamin Schreiber received a Ph.D. from the University of Würzburg, Germany, 2018, and BSc and MSc degrees in physics from TU Dresden, Germany. His research interests are focused on light intensifying photonic nanostructures for applications in biomedicine. He designed plasmonic systems for applications in SERS, detection of single molecule fluorescence, and recording the dynamics of G-Protein-coupled receptor *via*surface enhanced FRET. Theoretical and practical development of new optical instrumentation, especially for imaging and spectroscopy, had become his passion what he intensified during research stays at the Vienna Biocentre, Austria. Now, Benjamin is working in research and development for Carl Zeiss Meditec AG in Berlin, Germany, with focus on novel ophthalmological implants.

Prof. Habil. Dr. Arunas Ramanavicius is a professor and head of Department of Physical Chemistry at faculty of Chemistry of Vilnius University. He is also leading the laboratory of NanoTechnology at Research Center of Physical Sciences and Technologies. Prof. Arunas Ramanavicius is a member of Lithuanian Academy of sciences. In 1998 he received PhD degree and in 2002 doctor habilitus degree from Vilnius University. Prof. A. Ramanavicius is serving as expert-evaluator in Horizon 2020 program coordinated by European Commission and he is technical advisor of many foundations located in European and non-European countries. He has research interests in various aspects of nanotechnology, bionanotechnology, nanomaterials, biosensorics, bioelectronics, biofuel cells and MEMS based analytical devices. He is/was a national coordinator of several nanotechnology-related COST actions.

Prof. Dr. Dr. h.c. Dietrich RT Zahn (born 1958) studied Physics at RWTH Aachen and received a PhD degree in 1988 from the University of Wales in Cardiff. After a postdoc period at the TU Berlin he became Professor for Semiconductor Physics at the Technische Universität Chemnitz in 1993. His research interests focus on the spectroscopic characterisation of semiconductor surfaces, interfaces, ultra-thin films, and low-dimensional structures (> 800 publications, h-index 45). He served as Pro-rector for Research at the Technische Universität Chemnitz and as Head of the Thin Film Division of the German Physical Society (DFG). He was Speaker of the DFG Research Unit FOR 1154 “Towards Molecular Spintronics” and the DFG Research Unit FOR 1713 “Sensorical Micro and Nano Systems” and was member of the excellence clusters “MERGE” and “cfaed”. Prof. Zahn is Vice-president of the German Vacuum Society (DVG).

Prof. Dr. Evgeniya Sheremet was awarded a Ph.D. from Chemnitz University of Technology in Experimental Physics in 2015 for her thesis in “Micro- and nano-Raman characterization organic and inorganic materials”. Then she continued her work on nanocharacterization including finite element simulations of the electromagnetic field in the Solid Surfaces Analysis group of TU Chemnitz. From 2017 she became a full Professor at Tomsk Polytechnic University, Russia, where she continues her work in the field of nanospectroscopy and its bioapplications.